Magn. Reson., 2, 161–173, 2021
https://doi.org/10.5194/mr-2-161-2021

Open Access
MAGNETIC RESONANCE

The decay of the refocused Hahn echo in double electron–electron resonance (DEER) experiments

Thorsten Bahrenberg[1,★], **Samuel M. Jahn**[2,★], **Akiva Feintuch**[1], **Stefan Stoll**[2], **and Daniella Goldfarb**[1]

[1]Department of Chemical and Biological Physics, Weizmann Institute of Science, Rehovot 7610001, Israel
[2]Department of Chemistry, University of Washington, Seattle, Washington 98195, USA
★These authors contributed equally to this work.

Correspondence: Stefan Stoll (stst@uw.edu) and Daniella Goldfarb (daniella.goldfarb@weizmann.ac.il)

Received: 19 January 2021 – Discussion started: 26 January 2021
Revised: 4 March 2021 – Accepted: 13 March 2021 – Published: 16 April 2021

Abstract. Double electron–electron resonance (DEER) is a pulse electron paramagnetic resonance (EPR) technique that measures distances between paramagnetic centres. It utilizes a four-pulse sequence based on the refocused Hahn spin echo. The echo decays with increasing pulse sequence length $2(\tau_1+\tau_2)$, where τ_1 and τ_2 are the two time delays. In DEER, the value of τ_2 is determined by the longest inter-spin distance that needs to be resolved, and τ_1 is adjusted to maximize the echo amplitude and, thus, sensitivity. We show experimentally that, for typical spin centres (nitroxyl, trityl, and Gd(III)) diluted in frozen protonated solvents, the largest refocused echo amplitude for a given τ_2 is obtained neither at very short τ_1 (which minimizes the pulse sequence length) nor at $\tau_1=\tau_2$ (which maximizes dynamic decoupling for a given total sequence length) but rather at τ_1 values smaller than τ_2. Large-scale spin dynamics simulations based on the coupled cluster expansion (CCE), including the electron spin and several hundred neighbouring protons, reproduce the experimentally observed behaviour almost quantitatively. They show that electron spin dephasing is driven by solvent protons via the flip-flop coupling among themselves and their hyperfine couplings to the electron spin.

1 Introduction

DEER (double electron–electron resonance) spectroscopy is a highly effective method for nanometer-scale distance measurements in bio-macromolecules such as proteins, nucleic acids, and their complexes (Jeschke, 2013; Jeschke and Polyhach, 2007). This method measures the magnetic dipolar coupling between two spin labels attached at well-defined, specific locations in the bio-macromolecules. As the dipolar coupling strength is inversely proportional to the cube of the inter-spin distance, the distance distribution between the two spin labels can be determined from the DEER signal.

The original implementation of the DEER experiment, as introduced by Milov et al. (1981, 1984), is referred to as three-pulse DEER (Fig. 1a). It employs the standard two-pulse (Hahn) echo at one frequency, ν_1, and an additional pump pulse at another frequency, ν_2, applied at time t after the first pulse. The echo amplitude is measured as a function of the pump pulse position t. This sequence suffers from instrumental artefacts near $t=0$ due to pulse overlap between the first pulse and the pump pulse. To eliminate these artefacts, the dead-time-free four-pulse DEER experiment was introduced by Spiess and co-workers (Fig. 1b; Martin et al., 1998; Pannier et al., 2000). This method utilizes an additional refocusing π pulse to generate the refocused echo instead of the Hahn echo, allowing the undistorted measurement of the echo around $t=0$. Again, the echo amplitude is measured as a function of pump pulse position, t. Currently, the four-pulse DEER sequence is the most widely used DEER experiment.

The echo decays as the pulse sequence length increases, and the timescale of this decay is characterized by T_M, called

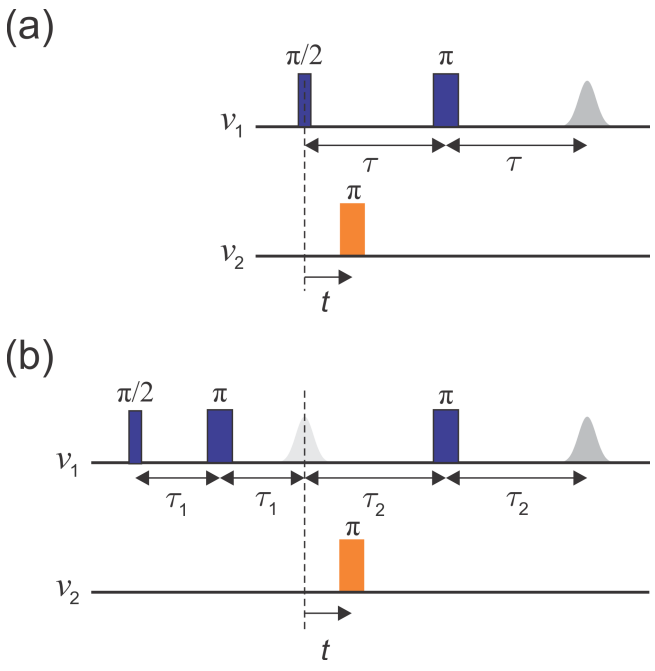

Figure 1. Schematics of **(a)** the three-pulse DEER sequence and **(b)** the dead-time-free four-pulse DEER sequence. Observer pulses are in blue and pump pulses in orange. The dashed line indicates $t = 0$.

the phase memory time or decoherence time. Long T_M values translate into high sensitivity. The longest possible pulse sequence length that still gives a sufficient echo amplitude determines the longest distance that can be resolved. Therefore, a long T_M is required to access long distances.

The DEER signal-to-noise ratio (SNR) depends on several factors that, for the three-pulse DEER, are approximately described by Jeschke and Polyhach (2007) and Zecevic et al. (1998) as follows:

$$\mathrm{SNR} \propto V_0 \lambda \frac{\mathrm{e}^{-(2\tau/T_M)^x}}{\sqrt{T_1}}, \quad (1)$$

where V_0 is the echo intensity at $\tau = 0$ (which is proportional to the number of spins in the sample), λ is the modulation depth and represents the fraction of spins inverted by the pump pulse, x is a stretching exponent, and T_1 is the spin–lattice relaxation time, which determines the rate of the data accumulation. Equation (1) is also applied in an approximate fashion for four-pulse DEER by replacing τ with $\tau_1 + \tau_2$ and setting $x = 1$ (Jeschke and Polyhach, 2007).

According to Eq. (1), for a fixed evolution time the sensitivity decreases exponentially with decreasing T_M. Therefore, one strives to prolong T_M as much as possible. It is possible to optimize the sample to suppress some of the mechanisms that contribute to dephasing. For example, the spin concentration can be lowered to minimize dephasing contributions due to electron–electron dipolar interactions, such as spectral and instantaneous diffusion (Eaton and Eaton, 2000, 2016; Raitsimring et al., 1974). However, this concentration reduction leads to a loss in absolute signal intensity and may significantly prolong the experiment runtime, and therefore, there is an optimal concentration for the best SNR (Jeschke and Polyhach, 2007). Another mechanism that strongly contributes to dephasing is nuclear spin diffusion, which is driven by magnetic nuclei that are coupled to the electron spin and among themselves (Brown, 1979; Canarie et al., 2020; Huber et al., 2001; Lenz et al., 2017; Milov et al., 1972; Mims, 1972; Salikhov and Tsvetkov, 1979; Zecevic et al., 1998). The dephasing by this mechanism is enhanced in particular by nuclei with a large gyromagnetic ratio, such as protons. Therefore, a reduction in the proton concentration leads to a longer T_M. This can be partially achieved by using deuterated solvents, which is a common practice nowadays (Jeschke and Polyhach, 2007), and – more completely but with more effort – by also deuterating the protein (El Mkami et al., 2014; Schmidt et al., 2016). Additionally, the contribution of nuclear-spin-driven dephasing can be reduced by the application of dynamic-decoupling schemes such as the Carr–Purcell (CP) sequence (Carr and Purcell, 1954), thus prolonging T_M (Harbridge et al., 2003). This concept was behind the design of the five-pulse (Borbat et al., 2013) and seven-pulse (Spindler et al., 2015) DEER sequences, which have been shown to allow significantly longer evolution times and access to longer distances. These experiments, however, are not straightforward to run because of the contribution of unwanted transfer pathways that generate additional signal contributions to the DEER trace (Breitgoff et al., 2017). The effect of dynamic decoupling on the dephasing of paramagnetic centres in frozen solutions and in solids has been investigated in several detailed studies (Kveder et al., 2019; Ma et al., 2014; Soetbeer et al., 2018, 2021).

A common practice for DEER is to record the two-pulse echo decay to estimate the maximum evolution time that can be applied for a particular sample. However, in the case of four-pulse DEER, a refocused two-pulse echo is observed, and therefore, it is the decay of this refocused echo which determines the SNR of the experiment and the distance accessibility. In the context of DEER, it is usually assumed that the refocused echo decays monotonically as a function of the overall pulse sequence length $2(\tau_1 + \tau_2)$, which is similar to the two-pulse echo. Based on this assumption, short τ_1 values are chosen to minimize dephasing during this initial interval. In this work, we show that this approach is not generally optimal, particularly in protonated solvents.

We explored the decay dependence of the refocused echo on τ_1 and τ_2, which is necessary for the optimization of the τ_1 values for achieving the best four-pulse DEER SNR. For this, we used the following three types of spin probes commonly used in DEER experiments on proteins: a common nitroxide radical, a trityl radical, and a Gd(III) complex (see Fig. 2), all in dilute frozen aqueous solutions. We show that, under conditions where the contribution of solvent nuclei to dephasing is significant (low concentrations and low tem-

peratures), the refocused echo sequence acts as a CP-like dynamic-decoupling sequence with two π pulses (Borbat et al., 2013). In this case, under the condition of a fixed and relatively long τ_2, necessary for DEER measurements, we find that the refocused echo intensity reaches its maximum at relatively long τ_1 values that are shorter than τ_2. This is in contrast to the common use of a short τ_1, chosen based on Eq. (1) to minimize the overall pulse sequence length. We present numerical spin dynamics simulations that reproduce the experimental results almost quantitatively and provide insight into the nature of dynamic decoupling in the refocused Hahn echo.

2 Methods

The 3-maleimido-proxyl and the trityl OXO63 were purchased from Sigma-Aldrich and from Oxford Instruments, respectively, and were used as provided. The powders were dissolved in either H_2O or D_2O to yield a 50 mM stock solution. They were further diluted using (a) a mixture of 80 % water and 20 % glycerol (v/v), (b) a mixture of 80 % D_2O and 20 % glycerol-d_8, or (c) mixtures thereof to create 25 %, 50 %, or 75 % deuterated solvents. The final radical concentration was 100 µM in all cases.

$GdCl_3$ was purchased from Sigma-Aldrich and used at a final concentration of 100 µM. The protein MdfA, labelled with Gd-C2 at positions 44 and 307 and solubilized in detergent, was prepared earlier according to a published protocol (Yardeni et al., 2019) and used without further modification. The final concentration of MdfA was about 25 µM.

Spectroscopic measurements. All measurements were carried out on a W-band (94.9 GHz), home-built spectrometer (Goldfarb et al., 2008; Mentink-Vigier et al., 2013). The two-pulse echo decays were recorded using the sequence shown in Fig. 1a, without the pump pulse, utilizing a two-step phase cycle. The two-dimensional refocused echo experiments were recorded using the sequence given in Fig. 1b, without the pump pulse, and the echo intensity was measured as a function of both τ_1 and τ_2. An eight-step-phase cycle of (x)(x)(x) was used (+/−x on all three pulses). Experimental parameters are listed in Table 1. In each case, the magnetic field was set to a value where the maximum of the EPR spectrum was resonant with the microwave frequency, unless stated otherwise. To produce the final signal, the echo was integrated over its full width at half maximum.

Simulations. To simulate the refocused echo decay, we follow our previously published approach (Canarie et al., 2020). A 3-maleimido-proxyl radical was geometry optimized, using density functional theory (DFT, B3LYP, and def2-SVP), and then solvated in a periodic box containing H_2O / glycerol (3038 waters and 188 glycerols), using molecular dynamics. The spin system used in the spin dynamics simulation includes the unpaired electron on the radical, all protons on the radical, and all protons from H_2O and glycerol molecules within 12 Å of the electron spin (512 protons total). The spin Hamiltonian includes full nucleus–nucleus coupling tensors and the secular and pseudo-secular parts of all $\hat{S}_z$–hyperfine coupling tensors ($\hat{S}_z\hat{I}_z$, $\hat{S}_z\hat{I}_x$, and $\hat{S}_z\hat{I}_y$) calculated from the electron and nucleus positions. The echo decay was simulated by explicit fully coherent time evolution of the spin system state, using density matrix propagation in Hilbert space, without any explicit relaxation terms. The calculations were performed using a truncated ensemble cluster correlation expansion (CCE; Yang and Liu, 2008, 2009), which is a refinement of the earlier cluster expansion (Witzel and Das Sarma, 2006). Echo signals from all possible subsystems involving the electron spin and a small cluster of nuclei are calculated separately, and the resulting signals are combined to give the total signal. To limit the number of clusters, we used a maximum nuclear cluster size of 2, 3, or 4 (2-CCE, 3-CCE, 4-CCE) and neglected all clusters with intra-cluster nucleus–nucleus couplings smaller than 1.58 kHz. This gave a converged signal and included 4365 two-proton clusters and 52 937 three-proton clusters. Orientational averaging was performed over a Lebedev grid with 14 points, taking the orientation-dependent excitation efficiency of the pulses into account. The simulations used an applied magnetic field of 3.38 T.

3 Results and discussion

To investigate the refocused echo decay, we acquired its amplitude as a function of both τ_1 and τ_2 for frozen solutions of a 3-maleimido-proxyl radical, the trityl OXO063, and Gd(III) (see Fig. 2). We measured all samples in both H_2O / glycerol (80 : 20, v/v) and D_2O / glycerol-d_8 (80 : 20, v/v) to examine the effect of nuclear spin diffusion. This is known to be a dominant mechanism of dephasing for organic radicals in dilute frozen solutions at cryogenic temperatures (Canarie et al., 2020; Eaton and Eaton, 2000; Zecevic et al., 1998) and has been shown to be partially suppressed using dynamic decoupling (Harbridge et al., 2003; Soetbeer et al., 2018, 2021).

3.1 Organic radicals

Figure 3a presents the measured refocused echo decay data of 3-maleimido-proxyl in H_2O / glycerol. It shows an overall monotonic decay as the values of τ_1 and τ_2 increase, and decay is symmetric with respect to exchange of τ_1 and τ_2. The data show that the echo decay is not a function of only the total pulse length, $2(\tau_1 + \tau_2)$, which is in contrast to the two-pulse echo decay. The decay is fastest along $\tau_1 \approx 0$ and $\tau_2 \approx 0$ and slowest along the diagonal $\tau_1 = \tau_2$. The latter is a manifestation of CP dynamic decoupling. While these general features of the decay are at least qualitatively as expected, the decay shape has a more subtle feature that has important practical implications for DEER measurements. In DEER, the choice of τ_2 is determined by the desired distance range, and an optimal choice of τ_1 maximizes the echo and,

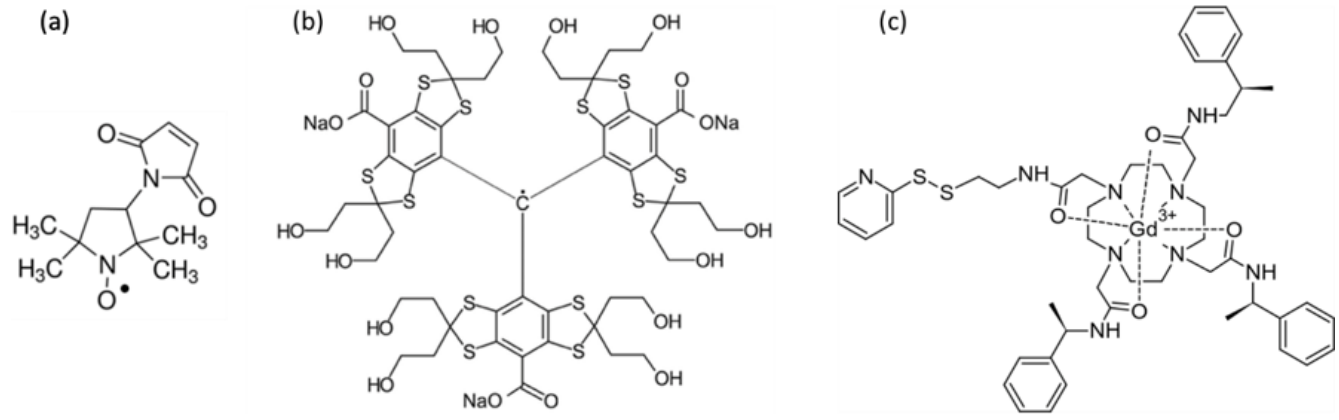

Figure 2. Chemical structures of the paramagnetic centres studied in this work, namely **(a)** 3-maleimido-proxyl, **(b)** trityl OXO63, and **(c)** Gd-C2.

Table 1. Experimental parameters used in this work. Identical parameters were used for the two-pulse and refocused echo measurements.

Sample	$\pi/2$ pulse (ns)	π pulse (ns)	Repetition time (ms)	Temperature (K)
3-maleimido-proxyl	25 or 20	50 or 40	20	25
trityl OXO63	25 or 20	50 or 40	100	25
Gd(III)*	15	30	0.3	10

* For both $GdCl_3$ and Gd-C2 labelled MdfA.

thereby, SNR. Optimizing τ_1 for a fixed τ_2 corresponds to finding the maximum along a particular horizontal slice of the data in Fig. 3a. This is more obvious in Fig. 3b, which shows the data from Fig. 3a after individual normalization of each horizontal τ_1-dependent trace with fixed τ_2. The superimposed red curve represent the loci of the maxima along these slices, corresponding to optimal τ_1 values for DEER. A similar plot and curve can be generated for vertical slices (fixed τ_1; variable τ_2), due to the symmetry of the decay across the $\tau_1 = \tau_2$ diagonal. The curves are also superimposed in Fig. 3a. The crucial feature of theses curves is their deviation from the diagonal ($\tau_1 = \tau_2$) for increasing values of τ_1 and τ_2.

Figure 3c shows individual slices at several τ_2 values (indicated in Fig. 3a and b by grey arrows), together with a two-pulse echo decay (dashed line) as reference. This shows that, in protonated solvents, the refocused echo decay along τ_1 (and, by symmetry, along τ_2) cannot generally be described by a stretched exponential decay. While there is little difference between the refocused echo decay and the two-pulse echo decay for small τ_2 values, for larger τ_2 values the refocused echo first grows significantly from its short-τ_1 amplitude, forms a broad maximum, and only then starts decaying. As a general trend, the longer the τ_2, the more pronounced the effect. This is relevant for DEER experiments, which are usually run with long τ_2 values to provide long dipolar evolution times. Interestingly, the maximum intensity does not appear at $\tau_1 = \tau_2$, where it would match the CP condition of maximal dynamic decoupling. Nor does it occur at $\tau_1 \approx 0$, corresponding to the minimal total pulse sequence length. Rather, it is slightly detuned from the CP diagonal and appears at $\tau_1 < \tau_2$. This deviation from the diagonal increases with increasing τ_2 values. In practice, for a DEER experiment in protonated solvents, this shows that setting τ_1 to a short value (to minimize total pulse sequence length), or equal to τ_2 (to maximize dynamic decoupling), leads to a significant and unnecessary loss of sensitivity. We observed this identical behaviour also at a magnetic field set to the region of g_{zz}, as shown (and in Fig. S1a–b in the Supplement). We also checked that the contributions of instantaneous diffusion under these conditions were negligible by comparing the Hahn echo decay obtained with different pulse lengths (see Fig. S1c).

Figure 4a shows the refocused echo decay for 3-maleimido-proxyl in the corresponding deuterated solvent. Here, both the Hahn echo and the refocused echo decays are significantly extended as compared to the protonated solvent, as expected, due to the absence of protons in the sample. The effect observed in protonated solvent is practically absent here. The echo amplitude depends only on the total pulse sequence length, $2(\tau_1 + \tau_2)$. The decays along τ_1 for fixed τ_2 are essentially independent of τ_2 and resemble very much the two-pulse echo decay (see Fig. 4b–c). It is apparent that nuclear spin diffusion is suppressed here, and dynamic

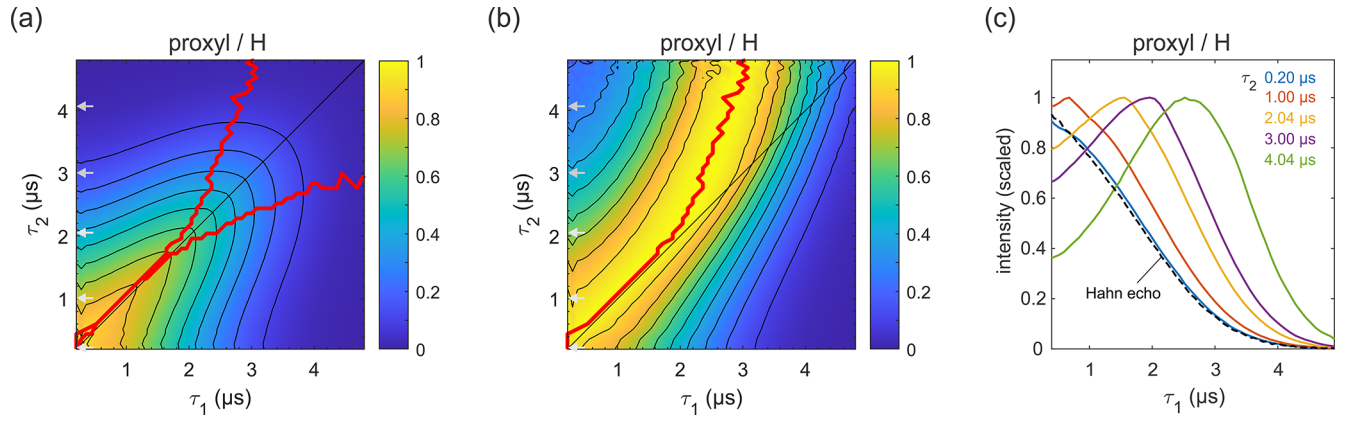

Figure 3. Refocused echo decay for 100 µM 3-maleimido-proxyl in H_2O / glycerol (80 : 20 v/v) at 25 K. Panel **(a)** shows the echo amplitude as a function of τ_1 and τ_2, and panel **(b)** shows the same data after normalization of each slice along τ_1. The red lines **(a, b)** indicate the location of the maxima along τ_1 for fixed τ_2 (upper line) and vice versa (lower line; only in **a**). Panel **(c)** shows slices along τ_1 for several τ_2 values (indicated by grey arrows in **a, b**), together with a Hahn echo decay.

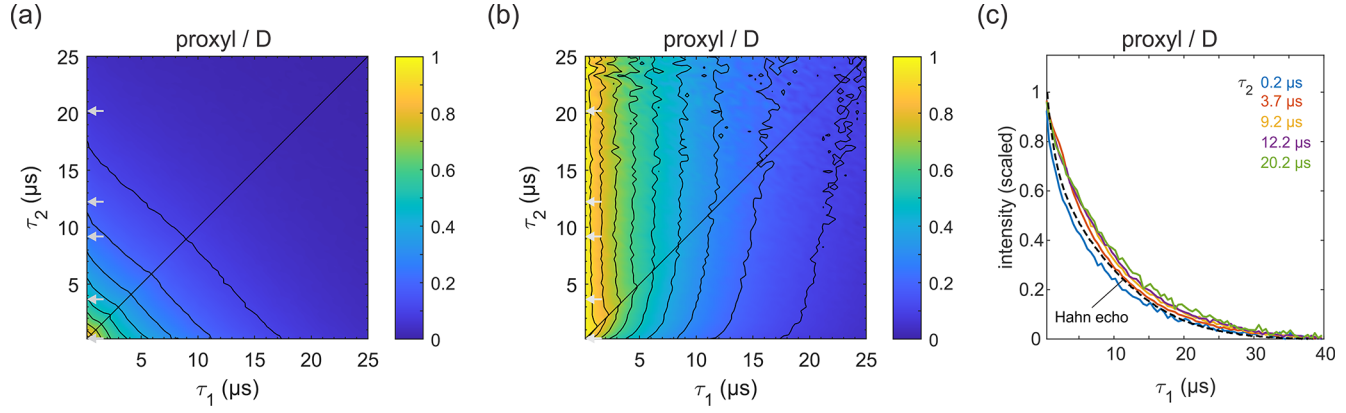

Figure 4. Refocused echo decay for 100 µM 3-maleimido-proxyl in D_2O / glycerol-d_8 (80 : 20 v/v) at 25 K. Panel **(a)** shows the echo amplitude as a function of τ_1 and τ_2, and panel **(b)** shows the same data after normalization of each slice along τ_1. Panel **(c)** shows slices along τ_1 for several τ_2 values (indicated by grey arrows in **a, b**), together with a Hahn echo decay.

decoupling is ineffective. The decay is dominated by other dephasing mechanisms such as instantaneous diffusion (Raitsimring et al., 1974) and therefore, a short τ_1 gives optimal sensitivity. It has recently been reported that, for a deuterated nitroxide attached to a model compound dissolved in 50 : 50 (v/v) D_2O / glycerol-d_8 or in deuterated o-terphenyl (OTP), the dynamic decoupling was efficient (Soetbeer et al., 2018, 2021). In this case, the protons on the large model compound generate a significant proton concentration in the vicinity of the nitroxide, which contributes to dephasing. We also note that the Hahn echo decays we observed do not reveal the significant fast echo decay component detected in the protonated and deuterated nitroxides in D_2O / glycerol-d_8 at low temperatures (10–50 K) that were reported recently (Soetbeer et al., 2021).

In order to evaluate how the degree of protonation affects the refocused echo decay shape, we measured samples in a partially deuterated solvent with 25 %, 50 %, and 75 % protonation. The results are shown in Fig. 5. These measurements reveal that, already at 25 % protonation, there is a strong impact on the decay timescale and shape, as can be seen by comparing Fig. 5a to Fig. 4a. At 50 % protonation, the effect is close to complete (Fig. 5b and c compared to Fig. 3a). The T_M values determined from two-pulse echo decays, given in Table 2, show a similar trend. They decrease with increasing proton concentration. The impact is strongest when going from 0 % protonation to 25 % and 50 % protonation. The differences between 50 %, 75 %, and 100 % protonation are smaller.

Figure 6 shows refocused echo decay data of the trityl OXO63, which is also used as a spin label for DEER on proteins and nucleic acids (Yang et al., 2012; Reginsson et al., 2012; Giannoulis et al., 2019). The data reveal the same behaviour as that observed for 3-maleimido-proxyl. Again, in a fully protonated solvent (Fig. 6a), the decay is fastest along $\tau_2 \approx 0$ and $\tau_1 \approx 0$, and it is slowest along the diagonal $\tau_1 =$

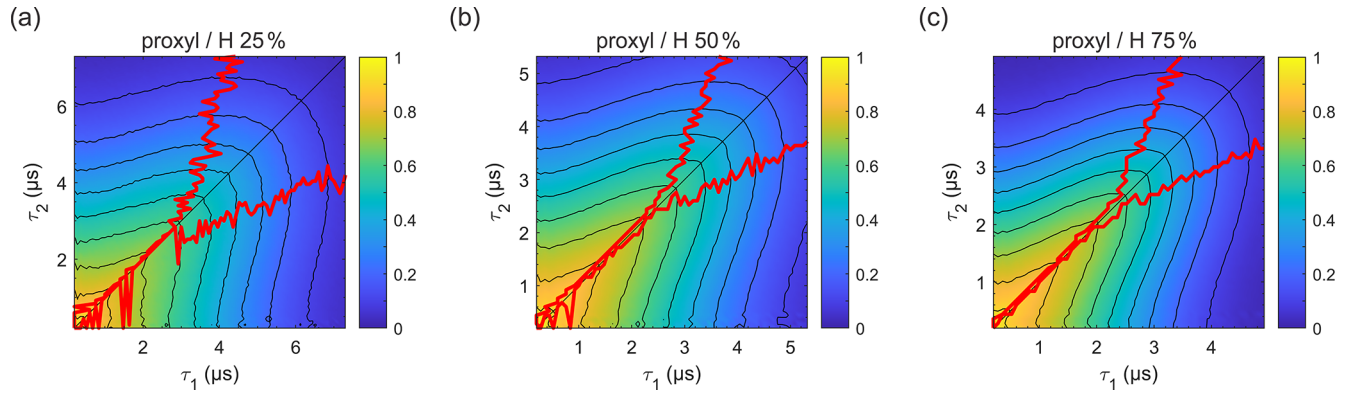

Figure 5. Refocused echo decay for 100 µM 3-maleimido-proxyl in H_2O / glycerol solvents (80 : 20 v/v) with varying degrees of solvent protonation at 25 K, i.e. **(a)** 25 %, **(b)** 50 %, and **(c)** 75 %. The red lines indicate the location of the maxima along τ_1 for fixed τ_2 (upper line) and vice versa (lower line). Plots for 100 % and 0 % solvent protonation are shown in Figs. 3a and 4a, respectively.

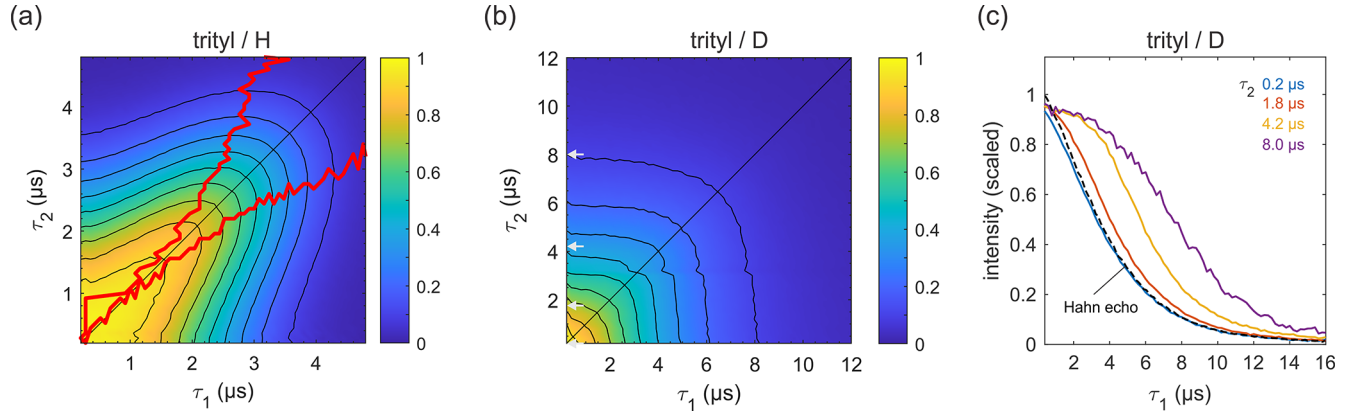

Figure 6. Refocused echo decays for 100 µM trityl OXO63 in **(a)** H_2O / glycerol (80 : 20 v/v) and **(b)** D_2O / glycerol-d_8 at 25 K; in panel **(a)**, the red lines show the position of the echo maximum along τ_1 for each constant τ_2 (upper line) and vice versa (lower line). Panel **(c)** shows slices of the data in panel **(b)** along τ_1 for several τ_2 values (indicated by grey arrows in **b**), together with a Hahn echo decay.

Table 2. The phase memory time, T_M, and the stretching exponent, x, obtained from fitting stretched exponential decays to the two-pulse echo decays (25 K) of the 3-maleimido-proxyl samples with different degrees of solvent protonation.

% Protonation	T_M (µs)	x
100	2.14(1)	2.01(2)
75	2.72(1)	2.11(2)
50	3.31(2)	1.99(2)
25	4.29(2)	1.91(3)
0	6.4(1)	0.65(1)

τ_2. The timescale is very similar to that of the 3-maleimido-proxyl decay. The asymmetry at short τ_1 and τ_2 is an experimental imperfection. Theoretically, in the high-temperature limit (which is applicable here), with ideal pulses (neglecting intra-pulse evolution), and for $T_1 \gg T_M$ (applicable here), one can show that the echo intensity is symmetric with respect to τ_1 and τ_2. As for 3-maleimido-proxyl, the location of the slice-wise maximum echo intensities (indicated by red lines) again deviates from the CP diagonal as τ_2 (or τ_1) increases. In contrast, in a fully deuterated solvent (Fig. 6b), no maxima in the echo intensities are observed, although there is a clear deviation from a pure $(\tau_1 + \tau_2)$-dependent decay as compared to 3-maleimido-proxyl in a deuterated solvent (Fig. 4). Figure 6c clearly shows that, as τ_2 increases, the echo intensity as a function of τ_1 persists longer. This indicates that nuclear spin diffusion, induced by the trityl OXO63 protons themselves, as reported recently (Soetbeer et al., 2021), is still a contributing mechanism, though not dominant enough to result in a non-monotonic behaviour as a function of τ_1.

3.2 Gd(III)

Next, we carried out similar measurements on high-spin Gd(III) ($S = 7/2$), as Gd(III)–Gd(III) DEER on proteins is

becoming more common (Feintuch et al., 2015). The results for $GdCl_3$ in protonated and deuterated solvents are shown in Fig. 7. In both solvents, the decay is essentially symmetric with respect to τ_1 and τ_2. In a protonated solvent (Fig. 7a), the shape of the 2D decay is generally similar to the ones observed for 3-maleimido-proxyl and trityl OXO63, except for short τ_1 and τ_2 with slice-wise echo maxima detuned from the CP condition (red lines). For small τ_2 values below about 1.5 µs, the optimal τ_1 is as short as possible, indicating that a second dephasing mechanism, in addition to nuclear spin diffusion, such as the transient zero field splitting mechanism, is contributing (Raitsimring et al., 2014). This is quite different from the organic radicals. In a deuterated solvent (Fig. 7b), the decay more closely resembles those observed for the organic radicals (Figs. 4a and 6b). As evident from Fig. 7c, proton nuclear spin diffusion, arising from protons on the Gd(III) ligand, plays a role in dephasing that is lower than in trityl OXO63 (Fig. 6c) but higher than in 3-maleimido-proxyl (Fig. 4c).

In all cases studied, a particularly interesting observation is the deviation of the maximum echo from the diagonal (the red lines in Figs. 3a, 5a, 6a, and 7a). For 3-maleimido-proxyl, the point at which the maxima starts to deviate from the diagonal is around $\tau_1 = 1.5$ µs for 100 % protonation and increases to about 2.7 µs for 25 % protonation. The deviation point for trityl OXO63 is similar, but for Gd(III) the behaviour is different, and the maximum echo is never observed along the diagonal, even for short τ_1 and τ_2. This general non-monotonic behaviour contrasts with the usual assumption of a monotonic decay and is rationalized as a balance between two competing effects that occur as τ_1 is increased from 0 to τ_2, leading to increased dephasing due to extending the pulse sequence length, on the one hand, and, on the other hand, the gain in amplitude due to the increasing degree of dynamic decoupling as τ_1 approaches τ_2.

Most applications of DEER are carried out on samples with a deuterated solvent, typically a mixture of D_2O / buffer and glycerol-d_8. However, complete deuteration is rarely achieved, as the buffer, substrates, detergent, lipid membrane, and the protein or nucleic acid of interest contain non-exchangeable protons that can be in close proximity to the spin label. There are also cases in which proteins precipitate in D_2O (Verheul et al., 1998; Reslan and Kayser, 2018). As it is now clear that the echo decay is strongly influenced by the presence of even small amounts of protons in the sample, it is still advisable to optimize the value of τ_1, even if the sample is only partially protonated. An example for a sample with incomplete deuteration is the membrane protein MdfA V44C/V307C, doubly labelled with the Gd-C2 tag, where labelling positions are on the exposed periplasmic face of the protein (Yardeni et al., 2019). MdfA is protonated and, being a membrane protein, is solubilized in detergent (n-dodecyl-β-D-maltopyranoside – DDM) micelles, which have a long alkyl chain with non-exchangeable protons. Consequently, even at 100 % solvent deuteration, a significant fraction of protons is present in the sample, in close proximity to the labels. These protons are expected to affect dephasing, as noted earlier for spin labels in micelles and lipid bilayers (Dastvan et al., 2010). Figure 8 shows the measured refocused echo decay as a function of τ_1 for selected fixed τ_2 times. The non-monotonic behaviour at the largest τ_2 is qualitatively similar to that observed for the organic radicals and $GdCl_3$. While the maximum is not as pronounced, this behaviour still has practical implications. The dipolar evolution time of DEER is typically in the range of 3–4 µs (yellow and purple traces), so τ_1 can safely be extended to almost 3 µs without a loss of sensitivity. This was exploited, for example, to remove instrumental artefacts from the DEER trace when shaped pulses are used (Bahrenberg et al., 2019).

3.3 Simulations

To better understand the physical origin of the observed refocused echo decay, we performed a numerical quantum spin dynamics simulation for a 3-maleimido-proxyl radical solvated in H_2O / glycerol as a representative of the behaviour observed experimentally. The molecular and solvation geometries were determined by DFT and molecular dynamics, respectively. The fully coherent spin dynamics simulation included the unpaired electron on the radical and all 512 protons within 12 Å of the unpaired electron. All $\hat{S}_z$–hyperfine and nucleus–nucleus coupling terms were included in the spin Hamiltonian. To handle the large Hilbert space with 2^{513} spin states, a truncated ensemble correlated cluster expansion (CCE) approach was utilized (see Sect. 2). This methodology has recently been shown to accurately reproduce the two-pulse echo decays of organic radicals in frozen, dilute protonated solutions (Canarie et al., 2020).

The simulated refocused echo decay is shown in Fig. 9a and b. Remarkably, it almost quantitatively matches the experimental result (Fig. 3a and b) both in shape and timescale, in particular with respect to the deviation of the maxima from the diagonal for long τ_1 and τ_2. A direct comparison with the experiment is shown in Fig. S2, where the largest deviation of the theory from experiment occurs for very short τ_2. The simulations show that the only terms in the spin Hamiltonian affecting the decay are the secular parts of the hyperfine couplings and the flip-flop terms of the nucleus–nucleus coupling (data not shown). In contrast, if the nucleus–nucleus couplings are neglected, the effect disappears. This is shown in Fig. 9c; if only one-nucleus clusters are included, namely, all nucleus–nucleus couplings are neglected, then no decay is seen. The shallow modulations are due to pseudo-secular components of the hyperfine couplings. Including two-nucleus clusters in the simulation yields an echo decay that has the correct shape and a timescale of the correct order of magnitude. Adding three-nucleus clusters improves the timescale slightly, and including larger clusters does not lead to further improvements. Water and H_2O / glycerol have very similar proton concentrations, so the decays are ex-

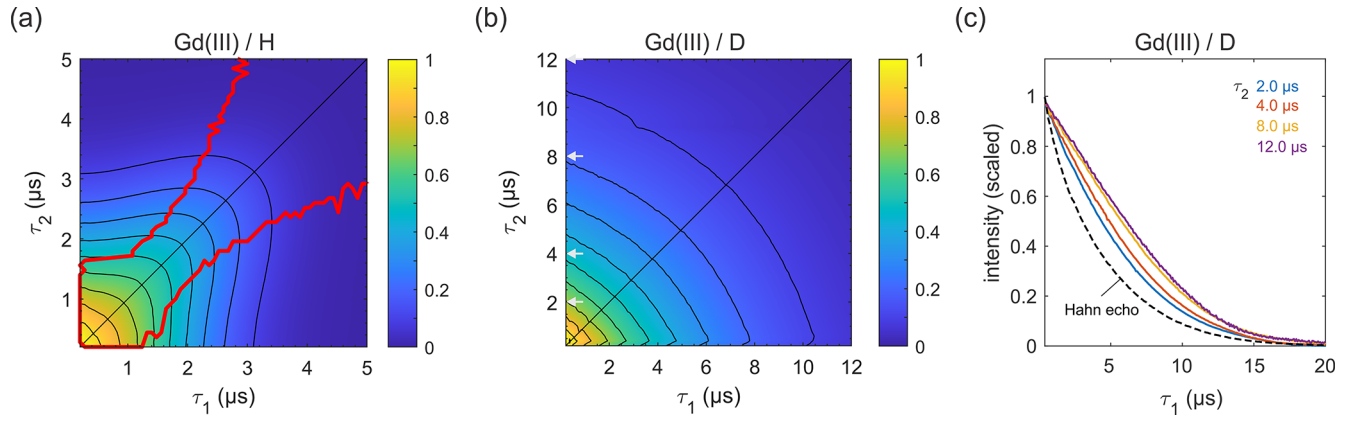

Figure 7. Refocused echo decays for 100 µM $GdCl_3$ in **(a)** H_2O / glycerol (80 : 20 v/v) and **(b)** D_2O / glycerol-d_8 at 10 K; in panel **(a)**, the red lines show the position of the echo maximum along τ_1 for each constant τ_2 (upper line) and vice versa (lower line). Grey arrows in **(b)** indicate the τ_2 values of slices shown in **(c)**, together with a Hahn echo decay.

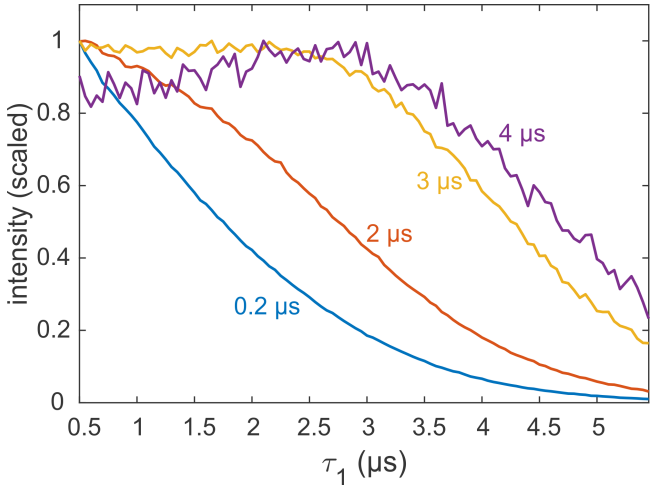

Figure 8. Refocused echo decay experiments (constant τ_2; variable τ_1) on 25 µM MdfA V44C/V307C, doubly labelled with Gd-C2, at 10 K. Selected values for τ_2 in nanoseconds are colour coded. Data taken from the Supplement of Yardeni et al. (2019).

pected to be similar. Indeed, simulations comparing water and H_2O / glycerol mixtures show that the two matrices give very similar results (see Fig. S3).

The conceptual essence of the mechanism can be pictured with one electron and a pair of nuclei, all coupled among each other. The associated three-spin system has eight eigenstates, with four nuclear eigenstates in each of the two electron spin manifolds (α and β). Due to presence of the flip-flop term of the nucleus–nucleus coupling, the nuclear eigenstates in the α manifold are different from those in the β manifold (assuming the two hyperfine couplings are not identical), and formally forbidden EPR transitions with $\Delta m_I \neq 0$ have non-zero transition amplitudes. Excitation of the system from one of its eigenstates in one manifold into the other manifold therefore generates nuclear coherence. This results in a periodic modulation of the electron spin echo amplitude as a function of inter-pulse delays, in a fashion analogous to electron spin echo envelope modulation (ESEEM; Van Doorslaer, 2017; Schweiger and Jeschke, 2001). Every cluster of nuclei contributes such a periodic modulation to the overall echo, with varying amplitudes and frequencies, depending on the structure of the cluster and its location relative to the electron spin. The solvent environment of the electron spin on the radical contains many nuclear clusters, and the echo modulations from all clusters combine to give an overall echo decay. Although the echo decays, the coherence lives on until it is destroyed by electron and nuclear T_1 relaxation processes.

Traditionally, this dephasing mechanism has been explained in terms of a stochastic nuclear spin diffusion model that involves flip-flop events between pairs of nuclei with a phenomenological flip-flop rate constant (Milov et al., 1973; Zecevic et al., 1998). However, the first-principles simulation shown earlier (Canarie et al., 2020) and here reveals that the term diffusion might not be entirely appropriate, as the quantum model that reproduces the echo decays is fully coherent and does not contain any relaxation terms or other stochastic elements. It might, therefore, be conceptually more accurate to refer to this dephasing mechanism as nuclear-spin-bath-driven electron spin decoherence, although this is clearly more tedious. It has been shown that the effect is field independent (no change between X and Q bands; Canarie et al., 2020). Also, theoretical considerations of a simple system of one electron spin and two spin-1/2 nuclei (Witzel and Das Sarma, 2006) show that the effect is independent of the field and depends only on the ratio of the nucleus–nucleus coupling to the difference in the two hyperfine couplings. We demonstrate this also for the refocused echo decay, where we compare simulations for W band versus Q band (see Fig. S4), which show that the only difference is in the ESEEM mod-

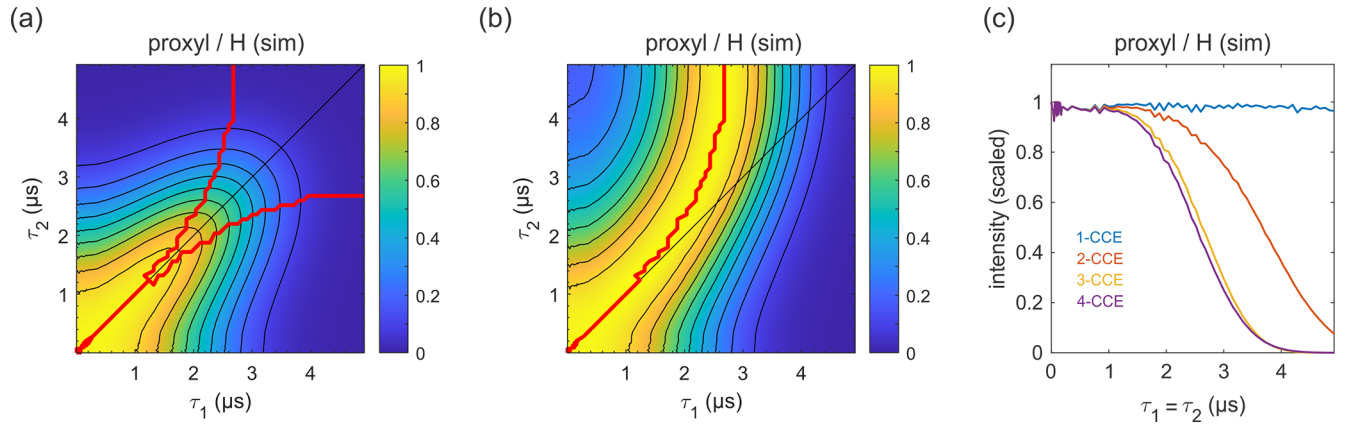

Figure 9. Simulation of the refocused echo decay for 3-maleimido-proxyl in H_2O / glycerol (80 : 20 v/v). Panel **(a)** shows the simulated refocused echo amplitude as a function of τ_1 and τ_2, using 3-CCE. The $\tau_1 = \tau_2$ line is shown in black. The upper red curve in panel **(a)** indicates the ridge of panel **(b)**, which normalizes each slice along τ_1 (with constant τ_2) to unit maximal amplitude. The lower red curve in panel **(a)** is the analogous ridge for normalization along τ_2. Panel **(c)** shows the simulated refocused echo decay for $\tau_1 = \tau_2$ as a function of cluster truncation level (1-CCE through 4-CCE).

ulations, and that the nuclear-spin-bath-driven dephasing is field independent.

The dynamic decoupling effect in the refocused echo decay, i.e. the decoherence suppression along $\tau_1 = \tau_2$, can be understood a little better with the simplified model Hamiltonian as follows:

$$\hat{H} = \mu_B g_e B_0 \hat{S}_z + \hbar \sum_n \left(-\mu_N g_n B_0 \hat{I}_{zn} + A_n \hat{S}_z \hat{I}_{zn} \right) + \hbar \sum_{m<n} b_{mn} \left(\hat{I}_{+m} \hat{I}_{-n} + \hat{I}_{-m} \hat{I}_{+n} - 4 \hat{I}_{zm} \hat{I}_{zn} \right), \quad (2)$$

where all symbols have their usual meaning. In particular, A_n represents the secular hyperfine coupling of nucleus n. The last sum contains the secular and flip-flop components of the couplings between nuclei m and n, with coupling parameter b_{nm}. Note that, in this Hamiltonian, the pseudo-secular hyperfine terms are omitted; however, they are included in all CCE simulations. Calculating the refocused echo amplitude $V(\tau_1, \tau_2)$, using density matrix propagation with ideal pulses, and Taylor expanding the resulting expression in terms of b_{mn} gives a power series where the lowest order non-vanishing term is second order in b_{mn} as follows:

$$\langle V_2 \rangle = -\sum_{m \neq n} \frac{2 b_{mn}^2}{\omega_{mn}^2} [\cos(\omega_{mn} \tau_1) - \cos(\omega_{mn} \tau_2)]^2, \quad (3)$$

where $\omega_{mn} = (A_m - A_n)/2$. This term is negative for $\tau_1 \neq \tau_2$ and zero for $\tau_1 = \tau_2$. $\langle V_2 \rangle$ also occurs as a factor to all higher-order terms in the power series. Factoring these out gives the power series for the exponential function, so that $\langle V_2 \rangle$ contributes a factor of $e^{\langle V_2 \rangle}$ to the overall echo amplitude. In general, each term in the Taylor series can be factored into terms that can be collected into exponentials, yielding the following:

$$V(\tau_1, \tau_2) = e^{\langle V_2 \rangle + \langle V_3 \rangle + \cdots} = e^{\langle V_2 \rangle} \cdot f(\tau_1, \tau_2), \quad (4)$$

where $\langle V_3 \rangle$ is the term cubic in b_{mn}, and we have collected all terms of orders higher than 2 in b_{nm} into a single term, f. This factorization is referred to as the linked-cluster expansion (Saikin et al., 2007).

Under the CP condition of $\tau_1 = \tau_2$, $\langle V_2 \rangle$ vanishes and, therefore, $e^{\langle V_2 \rangle} = 1$. The third-order term $e^{\langle V_3 \rangle}$ is negligible, leaving the fourth-order term as the lowest non-trivial term (Ma et al., 2014). Deviating from the $\tau_1 = \tau_2$ line introduces a non-zero negative second-order term and, therefore, $e^{\langle V_2 \rangle} < 1$. The significant three-spin terms are at least fourth order in b_{nm} and so are less significant when the second-order term contributes. This partially explains why three clusters in the simulations compress $V(\tau_1, \tau_2)$ along the $\tau_1 = \tau_2$ line – the CP effect breaks down at the same order that the three clusters start to contribute (Ma et al., 2014).

Maximizing echo intensity at a given τ_2 requires determining a τ_1 value that balances the loss from that which is deviating from the CP condition (quadratic in b_{nm}) with the loss from a long total experiment (quartic in b_{nm}).

Figure 10 illustrates the two factors $e^{\langle V_2 \rangle}$ and f for the 3-maleimido-proxyl case and CCE simulations up to 4-CCE in both standard and slice-wise normalized forms. It can be seen that $e^{\langle V_2 \rangle}$ accounts for most of the CP effect (Fig. 10a; top) that f represents, predominantly, the decay along $\tau_1 + \tau_2$ (Fig. 10a; bottom), and that 3-nucleus clusters contribute most to the part of f that drives the slice-wise maximum away from $\tau_1 = \tau_2$ (slice-wise diagrams; Fig. 10b; bottom).

Using the calculated shapes of $e^{\langle V_2 \rangle}$ and f in Fig. 10, we can rationalize the existence of a maximum of $V(\tau_1, \tau_2)$ along τ_1 for fixed τ_2, i.e. why we observe $\partial V / \partial \tau_1 = 0$ for some $0 < \tau_1 < \tau_2$. The derivative is as follows:

$$\frac{\partial V(\tau_1, \tau_2)}{\partial \tau_1} = e^{\langle V_2 \rangle} \frac{\partial f}{\partial \tau_1} + V(\tau_1, \tau_2) \frac{\partial \langle V_2 \rangle}{\partial \tau_1}. \quad (5)$$

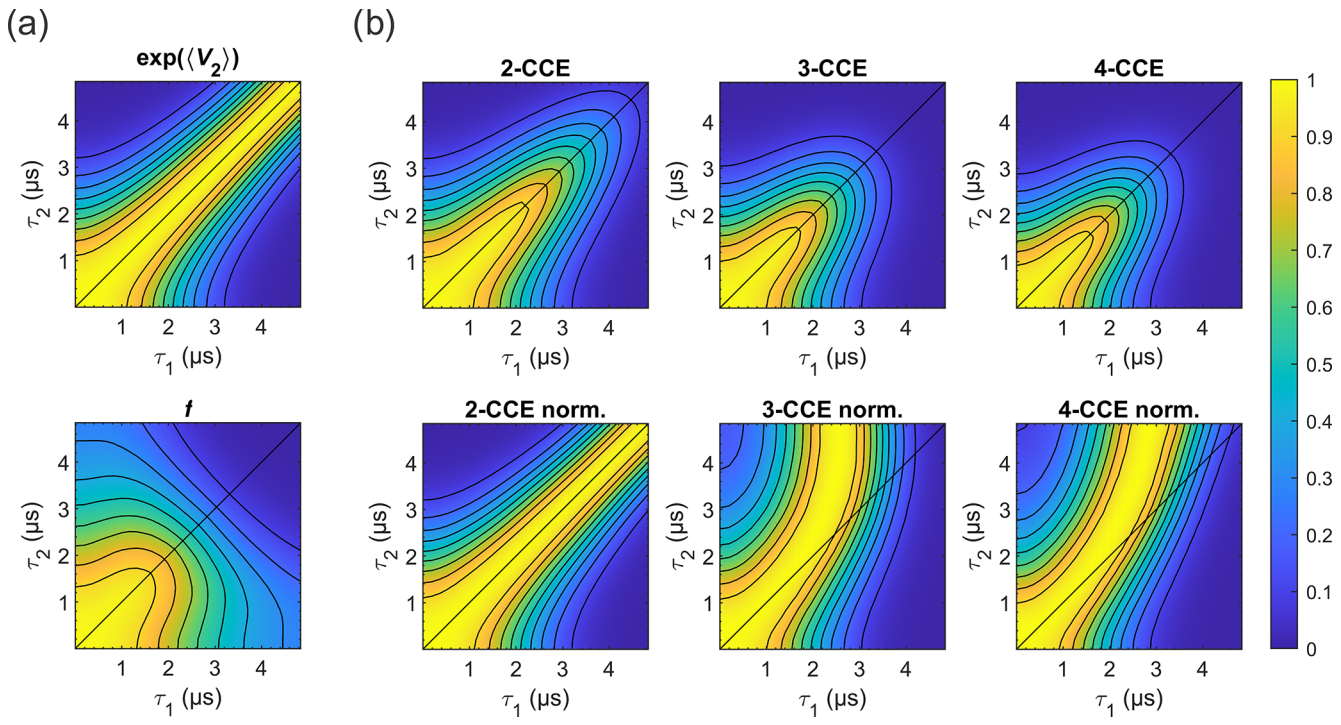

Figure 10. Simulated refocused echo decay of 3-maleimido-proxyl. **(a)** Factorization of the four-cluster decay into a second-order term in b_{nm} (top) and all higher-order terms (bottom). **(b)** Simulated refocused echo decays at two-, three-, and four-cluster level (2-CCE, 3-CCE, and 4-CCE; top), with the corresponding slice-wise normalized decays (bottom). For this simulation, a single orientation of the radical was used.

At $\tau_1 = \tau_2$, both derivatives on the right-hand side are negative (as seen in Fig. 10), rendering $\partial V/\partial\tau_1$ negative – increasing τ_1 beyond τ_2 always decreases the echo, since the CP suppression is lost and the total evolution time becomes longer. In addition, for a given τ_2, and for some region $\tau_1 < \tau_2$, $e^{\langle V_2\rangle}$ grows more rapidly with τ_1 than f decays with τ_1, as seen in Fig. 10. Therefore, $\partial V/\partial\tau_1 > 0$, which indicates that there is at least one τ_1 for which an increase in τ_1 increases V. This is related to the Taylor series converging fast enough. An increase in V with τ_1 indicates the gain in echo amplitude from approaching the CP condition is larger than the loss from prolonging the total evolution time. Taken together, this means that $\partial V/\partial\tau_1$ must be zero for some $\tau_1 < \tau_2$ and, therefore, V maximal. At that point, the effects of increasing $e^{\langle V_2\rangle}$ (signal gain due to better dynamic decoupling) and decreasing f (signal loss due to longer evolution time) are balanced.

4 Conclusions

We observe that, for low-concentration nitroxide, trityl and Gd(III) paramagnetic centres in protonated solvents, where the so-called nuclear spin diffusion decoherence mechanism dominates, the refocused two-pulse echo amplitude as a function of τ_1 for a fixed τ_2 was neither maximal for $\tau_1 = 0$ (which minimizes total pulse sequence duration) nor $\tau_1 = \tau_2$ (which maximizes dynamic decoupling given a fixed total pulse sequence duration) but rather for a τ_1 value between 0 and τ_2. We observed this effect in samples with 25 %–100 % solvent protonation. In fully deuterated solvents, the effect was not observed owing to fact that other dephasing mechanisms (such as instantaneous diffusion) become significant or dominant, at least at the concentrations employed in this study.

First-principle spin dynamics simulations, using a solvated nitroxide radical structure, reproduced both the timescale and the shape of the observed refocused echo decay, indicating that it is due to the large number of protons proximal to the spin label. This confirms that nuclear-spin-driven decoherence is the main mechanism of echo decay in the protonated samples under the conditions investigated (low concentration and low temperature). Although in this work we focused on the decay of the refocused echo as a function of the time intervals τ_1 and τ_2, it is interesting to compare our Hahn echo decay shapes with those reported earlier by Soetbeer et al. (2018), where the data were analysed in terms of a sum of two stretched exponentials – one with a fast decay and another with a slow decay. We do not observe the fast decay, which was particularly prominent in the protonated and deuterated nitroxides in D_2O / glycerol-d_8 at low temperatures (10–50 K; Soetbeer et al., 2021). Similarly, this was not observed in our earlier report on trityl, nitroxide, and Gd(III)

spin labels as being free and attached to a protein (Yang et al., 2020). The difference could be due to the field (Q band vs W band) or the different type of nitroxide used.

These findings have practical implications for DEER experiments. There, τ_2 is typically determined by structural considerations, such as the longest distances that need to be resolved. The choice of τ_1 that maximizes SNR for a given τ_2 is therefore important. Our results indicate that it is important to explore the entire range of possible τ_1 values in order to find the maximum SNR for the DEER measurement, in particular for samples that cannot be produced with 100 % deuteration of all components (solvent, protein, detergent, etc.).

Code and data availability. All measured data are available at https://doi.org/10.5281/zenodo.4449018 (Bahrenberg et al., 2021).

Supplement. The supplement related to this article is available online at: https://doi.org/10.5194/mr-2-161-2021-supplement.

Author contributions. TB, AF, and DG initiated the project. TB, SMJ, AF, SS, and DG designed the research. TB performed all experiments and analysed the data. SMJ implemented the code and performed all simulations. All authors wrote the paper.

Competing interests. The authors declare that they have no conflict of interest.

Acknowledgements. This research was made possible in part by the historic generosity of the Harold Perlman family (Daniella Goldfarb). Daniella Goldfarb holds the Erich Klieger professorial chair in chemical physics.

Financial support. This research has been supported by the Minerva Foundation (grant no. 713223; Daniella Goldfarb) and the National Institutes of Health (grant no. R01 GM125753; Stefan Stoll).

Review statement. This paper was edited by Tatyana Polenova and reviewed by Mike Bowman, Thomas Prisner, and one anonymous referee.

References

Bahrenberg, T., Yang, Y., Goldfarb, D., and Feintuch, A.: rDEER: A Modified DEER Sequence for Distance Measurements Using Shaped Pulses, Magnetochemistry, 5, 20, https://doi.org/10.3390/magnetochemistry5010020, 2019.

Bahrenberg, T., Jahn, S. M., Feintuch, A., Stoll, S., and Goldfarb, D.: The decay of the refocused Hahn echo in DEER experiments, Raw data, Zenodo, https://doi.org/10.5281/zenodo.4449018, 2021.

Borbat, P. P., Georgieva, E. R., and Freed, J. H.: Improved sensitivity for long-distance measurements in biomolecules: Five-pulse double electron-electron resonance, J. Phys. Chem. Lett., 4, 170–175, https://doi.org/10.1021/jz301788n, 2013.

Breitgoff, F. D., Soetbeer, J., Doll, A., Jeschke, G., and Polyhach, Y. O.: Artefact suppression in 5-pulse double electron electron resonance for distance distribution measurements, Phys. Chem. Chem. Phys., 19, 15766–15779, https://doi.org/10.1039/c7cp01488k, 2017.

Brown, I.: Electron spin-echo studies of relaxation processes in molecular solids, in: Time Domain Electron Spin Resonance, edited by: Kevan, L. and Schwartz, R. N., John Wiley & Sons, New York, 195–229, 1979.

Canarie, E. R., Jahn, S. M., and Stoll, S.: Quantitative Structure-Based Prediction of Electron Spin Decoherence in Organic Radicals, J. Phys. Chem. Lett., 11, 3396–3400, https://doi.org/10.1021/acs.jpclett.0c00768, 2020.

Carr, H. Y. and Purcell, E. M.: Effects of diffusion on free precession in nuclear magnetic resonance experiments, Phys. Rev., 94, 630–638, https://doi.org/10.1103/PhysRev.94.630, 1954.

Dastvan, R., Bode, B. E., Karuppiah, M. P. R., Marko, A., Lyubenova, S., Schwalbe, H., and Prisner, T. F.: Optimization of transversal relaxation of nitroxides for pulsed electron-electron double resonance spectroscopy in phospholipid membranes, J. Phys. Chem. B, 114, 13507–13516, https://doi.org/10.1021/jp1060039, 2010.

Eaton, S. S. and Eaton, G. R.: Relaxation mechanisms, eMagRes, 5, 1543–1556, https://doi.org/10.1002/9780470034590.emrstm1507, 2016.

Eaton, S. S. and Eaton, G. R.: Relaxation times of organic radicals and transition metal ions, in: Distance measurements in biological systems by EPR, edited by: Berliner, L., Eaton, S. S., and Eaton, G. R., Springer, Boston, MA, 19, 29–154, https://doi.org/10.1007/0-306-47109-4_2, 2000.

El Mkami, H., Ward, R., Bowman, A., Owen-Hughes, T., and Norman, D. G.: The spatial effect of protein deuteration on nitroxide spin-label relaxation: Implications for EPR distance measurement, J. Magn. Reson., 248, 36–41, https://doi.org/10.1016/J.JMR.2014.09.010, 2014.

Feintuch, A., Otting, G., and Goldfarb, D.: Gd^{3+} Spin Labeling for Measuring Distances in Biomacromolecules: Why and How?, Methods Enzymol., 563, 415–457, https://doi.org/10.1016/bs.mie.2015.07.006, 2015.

Giannoulis, A., Yang, Y., Gong, Y., Tan, X., Feintuch, A., Carmieli, R., Bahrenberg, T., Liu, Y., Su, X., and Goldfarb, D.: DEER distance measurements on trityl/trityl and Gd(iii)/trityl labelled proteins, Phys. Chem. Chem. Phys., 21, 10217–10227, https://doi.org/10.1039/c8cp07249c, 2019.

Goldfarb, D., Lipkin, Y., Potapov, A., Gorodetsky, Y., Epel, B., Raitsimring, A. M., Radoul, M., and Kaminker, I.: HYSCORE and DEER with an upgraded 95 GHz pulse EPR spectrometer, J. Magn. Reson., 194, 8–15, https://doi.org/10.1016/j.jmr.2008.05.019, 2008.

Harbridge, J. R., Eaton, S. S., and Eaton, G. R.: Comparison of electron spin relaxation times measured by Carr–Purcell–Meiboom–Gill and two-pulse spin-echo sequences, J. Magn. Reson., 164, 44–53, https://doi.org/10.1016/S1090-7807(03)00182-4, 2003.

Huber, M., Lindgren, M., Hammarström, P., Mårtensson, L.-G., Carlsson, U., Eaton, G. R., and Eaton, S. S.: Phase memory relaxation times of spin labels in human carbonic anhydrase II: pulsed EPR to determine spin label location, Biophys. Chem., 94, 245–256, https://doi.org/10.1016/S0301-4622(01)00239-3, 2001.

Jeschke, G.: Interpretation of Dipolar EPR Data in Terms of Protein Structure, in: Structural Information from Spin-Labels and Intrinsic Paramagnetic Centres in the Biosciences, edited by: Timmel, C. R. and Harmer, J. R., Springer, Berlin, Heidelberg, Germany, 83–120, 2013.

Jeschke, G. and Polyhach, Y.: Distance measurements on spin-labelled biomacromolecules by pulsed electron paramagnetic resonance, Phys. Chem. Chem. Phys., 9, 1895–1910, https://doi.org/10.1039/b614920k, 2007.

Kveder, M., Rakvin, B., and You, J.: A quantum many body model for the embedded electron spin decoherence in organic solids, J. Chem. Phys., 151, 164124, https://doi.org/10.1063/1.5124561, 2019.

Lenz, S., Bader, K., Bamberger, H., and Van Slageren, J.: Quantitative prediction of nuclear-spin-diffusion-limited coherence times of molecular quantum bits based on copper(ii), Chem. Commun., 53, 4477–4480, https://doi.org/10.1039/c6cc07813c, 2017.

Ma, W. L., Wolfowicz, G., Zhao, N., Li, S. S., Morton, J. J. L., and Liu, R. B.: Uncovering many-body correlations in nanoscale nuclear spin baths by central spin decoherence, Nat. Commun., 5, 4822, https://doi.org/10.1038/ncomms5822, 2014.

Martin, R. E., Pannier, M., Diederich, F., Gramlich, V., Hubrich, M., and Spiess, H. W.: Determination of End-to-End Distances in a Series of TEMPO Diradicals of up to 2.8 nm Length with a New Four-Pulse Double Electron Electron Resonance Experiment, Angew. Chem. Int. Edit., 37, 2833–2837, 1998.

Mentink-Vigier, F., Collauto, A., Feintuch, A., Kaminker, I., Tarle, V., and Goldfarb, D.: Increasing sensitivity of pulse EPR experiments using echo train detection schemes, J. Magn. Reson., 236, 117–125, https://doi.org/10.1016/j.jmr.2013.08.012, 2013.

Milov, A. D., Salikhov, K. M., and Tsvetkov, Y. D.: Spin diffusion and kinetics of spin-lattice relaxation of H-atoms in glassy matrices at 77 K, Fiz. Tverd. Tela, 14, 2211–2215, 1972.

Milov, A. D., Tsvetkov, Y. D., and Salikhov, K. M.: Phase relaxation of H-atoms stabilized in glassy matrices, Fiz. Tverd. Tela, 15, 1187–1195, 1973.

Milov, A. D., Salikhov, K. M., and Shirov, M. D.: Application of the double resonance method to electron spin echo in a study of the spatial distribution of paramagnetic centers in solids, Fiz. Tverd. Tela+, 23, 975–982, 1981.

Milov, A. D., Ponomarev, A. B., and Tsvetkov, Y. D.: Electron-electron double resonance in electron spin echo: Model biradical systems and the sensitized photolysis of decalin, Chem. Phys. Lett., 110, 67–72, https://doi.org/10.1016/0009-2614(84)80148-7, 1984.

Mims, W. B.: Electron spin echoes, in: Electron Paramagnetic Resonance, edited by: Geschwind, S., Plenum, New York, USA, 263–351, 1972.

Pannier, M., Veit, S., Godt, A., Jeschke, G., and Spiess, H. W.: Dead-Time Free Measurement of Dipole-Dipole Interactions between Electron Spins, J. Magn. Reson., 142, 331–340, https://doi.org/10.1006/jmre.1999.1944, 2000.

Raitsimring, A. M., Salikhov, K. M., Umanski, U., and Tsvetkov, Y. D.: The instantaneous diffusion of the ESE paramagnetic centers in solids, Fiz. Tverd. Tela+, 16, 756–763, 1974.

Raitsimring, A. M., Dalaloyan, A., Collauto, A., Feintuch, A., Meade, T., and Goldfarb, D.: Zero field splitting fluctuations induced phase relaxation of Gd^{3+} in frozen solutions at cryogenic temperatures, J. Magn. Reson., 248, 71–80, https://doi.org/10.1016/j.jmr.2014.09.012, 2014.

Reginsson, G. W., Kunjir, N. C., Sigurdsson, S. T., and Schiemann, O.: Trityl radicals: Spin labels for nanometer-distance measurements, Chem.-Eur. J., 18, 13580–13584, https://doi.org/10.1002/chem.201203014, 2012.

Reslan, M. and Kayser, V.: The effect of deuterium oxide on the conformational stability and aggregation of bovine serum albumin, Pharm. Dev. Technol., 23, 1030–1036, https://doi.org/10.1080/10837450.2016.1268157, 2018.

Saikin, S. K., Yao, W., and Sham, L. J.: Single-electron spin decoherence by nuclear spin bath: Linked-cluster expansion approach, Phys. Rev. B, 75, 125314, https://doi.org/10.1103/PhysRevB.75.125314, 2007.

Salikhov, K. M. and Tsvetkov, Y. D.: Electron spin-echo studies of spin-spin interactions in solids, in: Time Domain Electron Spin Resonance, edited by: Kevan, L. and Schwartz, R. N., Wiley, New York, USA, 279–341, 1979.

Schmidt, T., Wälti, M. A., Baber, J. L., Hustedt, E. J., and Clore, G. M.: Long Distance Measurements up to 160 Å in the GroEL Tetradecamer Using Q-Band DEER EPR Spectroscopy, Angew. Chem. Int. Edit., 55, 15905–15909, https://doi.org/10.1002/anie.201609617, 2016.

Schweiger, A. and Jeschke, G.: Principles of Pulse Electron Paramagnetic Resonance, Oxford University Press, Oxford, UK, 2001.

Soetbeer, J., Hülsmann, M., Godt, A., Polyhach, Y., and Jeschke, G.: Dynamical decoupling of nitroxides in: O-terphenyl: A study of temperature, deuteration and concentration effects, Phys. Chem. Chem. Phys., 20, 1615–1628, https://doi.org/10.1039/c7cp07074h, 2018.

Soetbeer, J., Millen, M., Zouboulis, K., Hülsmann, M., Godt, A., Polyhach, Y., and Jeschke, G.: Dynamical decoupling in water-glycerol glasses: a comparison of nitroxide, trityl and gadolinium radicals, Phys. Chem. Chem. Phys., 23, 5352–5369, https://doi.org/10.1039/d1cp00055a, 2021.

Spindler, P. E., Waclawska, I., Endeward, B., Plackmeyer, J., Ziegler, C., and Prisner, T. F.: Carr-Purcell Pulsed Electron Double Resonance with Shaped Inversion Pulses, J. Phys. Chem. Lett., 6, 4331–4335, https://doi.org/10.1021/acs.jpclett.5b01933, 2015.

Van Doorslaer, S.: Hyperfine spectroscopy: ESEEM, eMagRes, 6, 51–70, https://doi.org/10.1002/9780470034590.emrstm1517, 2017.

Verheul, M., Roefs, S. P. F. M., and de Kruif, K. G.: Aggregation of β-lactoglobulin and infuence of D_2O, FEBS Lett., 421, 273–276, 1998.

Witzel, W. M. and Das Sarma, S.: Quantum theory for electron spin decoherence induced by nuclear spin dynamics in semiconductor quantum computer architectures: Spectral diffusion of localized electron spins in the nuclear solid-state environment, Phys. Rev. B, 74, 035322, https://doi.org/10.1103/PhysRevB.74.035322, 2006.

Yang, W. and Liu, R. B.: Quantum many-body theory for qubit decoherence in a finite-size spin bath, AIP Conf. Proc., 1074, 68–71, https://doi.org/10.1063/1.3037140, 2008.

Yang, W. and Liu, R. B.: Quantum many-body theory of qubit decoherence in a finite-size spin bath, II. Ensemble dynamics, Phys. Rev. B, 79, 115320, https://doi.org/10.1103/PhysRevB.79.115320, 2009.

Yang, Y., Pan, B. Bin, Tan, X., Yang, F., Liu, Y., Su, X. C., and Goldfarb, D.: In-Cell Trityl-Trityl Distance Measurements on Proteins, J. Phys. Chem. Lett., 11, 1141–1147, https://doi.org/10.1021/acs.jpclett.9b03208, 2020.

Yang, Z., Liu, Y., Borbat, P., Zweier, J. L., Freed, J. H., and Hubbell, W. L.: Pulsed ESR dipolar spectroscopy for distance measurements in immobilized spin labeled proteins in liquid solution, J. Am. Chem. Soc., 134, 9950–9952, https://doi.org/10.1021/ja303791p, 2012.

Yardeni, E. H., Bahrenberg, T., Stein, R. A., Mishra, S., Zomot, E., Graham, B., Tuck, K. L., Huber, T., Bibi, E., Mchaourab, H. S., and Goldfarb, D.: Probing the solution structure of the E. coli multidrug transporter MdfA using DEER distance measurements with nitroxide and Gd(III) spin labels, Sci. Rep.-UK, 9, 12528, https://doi.org/10.1038/s41598-019-48694-0, 2019.

Zecevic, A., Eaton, G. R., Eaton, S. S., and Lindgren, M.: Dephasing of electron spin echoes for nitroxyl radicals in glassy solvents by non-methyl and methyl protons, Mol. Phys., 95, 1255–1263, 1998.